Thermocline Fluctuations in the Equatorial Pacific Related to the Two Types of El Niño Events

KANG XU

State Key Laboratory of Tropical Oceanography, South China Sea Institute of Oceanology, Chinese Academy of Science, Guangzhou, and State Key Laboratory of Numerical Modeling for Atmospheric Sciences and Geophysical Fluid Dynamics, Institute of Atmospheric Physics, Chinese Academy of Sciences, Beijing, China

RUI XIN HUANG

Woods Hole Oceanographic Institute, Woods Hole, Massachusetts, and State Key Laboratory of Tropical Oceanography, South China Sea Institute of Oceanology, Chinese Academy of Science, Guangzhou, China

WEIQIANG WANG

State Key Laboratory of Tropical Oceanography, South China Sea Institute of Oceanology, Chinese Academy of Science, Guangzhou, and Laboratory for Regional Oceanography and Numerical Modeling, Qingdao National Laboratory for Marine Science and Technology, Qingdao, China

CONGWEN ZHU

Institute of Climate System, Chinese Academy of Meteorological Sciences, Beijing, China

RIYU LU

State Key Laboratory of Numerical Modeling for Atmospheric Sciences and Geophysical Fluid Dynamics, Institute of Atmospheric Physics, Chinese Academy of Sciences, Beijing, China

(Manuscript received 8 April 2016, in final form 10 May 2017)

ABSTRACT

The interannual fluctuations of the equatorial thermocline are usually associated with El Niño activity, but the linkage between the thermocline modes and El Niño is still under debate. In the present study, a mode function decomposition method is applied to the equatorial Pacific thermocline, and the results show that the first two dominant modes (M1 and M2) identify two distinct characteristics of the equatorial Pacific thermocline. The M1 reflects a basinwide zonally tilted thermocline related to the eastern Pacific (EP) El Niño, with shoaling (deepening) in the western (eastern) equatorial Pacific. The M2 represents the central Pacific (CP) El Niño, characterized by a V-shaped equatorial Pacific thermocline (i.e., deep in the central equatorial Pacific and shallow on both the western and eastern boundaries). Furthermore, both modes are stable and significant on the interannual time scale, and manifest as the major feature of the thermocline fluctuations associated with the two types of El Niño events. As good proxies of EP and CP El Niño events, thermocline-based indices clearly reveal the inherent characteristics of subsurface ocean responses during the evolution of El Niño events, which are characterized by the remarkable zonal eastward propagation of equatorial subsurface ocean temperature anomalies, particularly during the CP El Niño. Further analysis of the mixed layer heat budget suggests that the air–sea interactions determine the establishment and development stages of the CP El Niño, while the thermocline feedback is vital for its further development. These results highlight the key influence of equatorial Pacific thermocline fluctuations in conjunction with the air–sea interactions, on the CP El Niño.

Corresponding author: Weiqiang Wang, weiqiang.wang@scsio.ac.cn.

DOI: 10.1175/JCLI-D-16-0291.1

1. Introduction

The equatorial thermocline is an essential component of oceanic circulation and the climate system. It acts as an invisible blanket, separating the very active upper-layer water from the relatively quiet and stagnant deep water below in the tropics. Its effects extend far beyond the tropics through both atmospheric and oceanic teleconnections, greatly affecting global society and natural systems (Pedlosky 1987; Gu and Philander 1997). On the interannual time scale, the equatorial Pacific thermocline is closely associated with El Niño–Southern Oscillation (ENSO), which results from the coupled ocean–atmosphere interactions in the tropical Pacific (McPhaden et al. 2006). Jin (1997) proposed the recharge oscillator mechanism including zonal advective feedback and thermocline feedback to illuminate the role of the upper-oceanic heat content in the ENSO cycle. Variations in the equatorial thermocline are accompanied by subsurface ocean temperature anomalies (SOTAs) along the equatorial thermocline; in fact, SOTAs lead ENSO sea surface temperature (SST) anomalies (SSTAs) in the eastern Pacific by at least two seasons (McPhaden et al. 2006). Therefore, variations in the SOTAs are regarded as the major predictor of ENSO (Meinen and McPhaden 2000).

Recent studies have revealed a new type of El Niño event emerging in the central tropical Pacific (Trenberth and Stepaniak 2001; Larkin and Harrison 2005; Ashok et al. 2007; Yu and Kao 2007; Kug et al. 2009; Ren and Jin 2011; Wang and Wang 2013). For this type of El Niño event, the strongest anomalous warming is located in the central equatorial Pacific, in contrast to the canonical El Niño with a warming center in the eastern equatorial Pacific (Ashok and Yamagata 2009; Zhang et al. 2014, 2015; Xu et al. 2017). Based on the locations of the warming center of SSTAs, these two types of El Niño events are referred to as the eastern Pacific (EP) and central Pacific (CP) El Niño events in the present study.

Although thermocline feedback has been validated as an important component of the conventional EP El Niño, there is no consensus on its effects on the CP El Niño. Some studies have emphasized the importance of equatorial Pacific thermocline fluctuations on the evolution of both the EP and CP El Niño events. For instance, Ashok et al. (2007) explored the role of the wind-forced equatorial thermocline variability in the evolution of CP El Niño events, and Kim et al. (2011) argued that strong thermocline anomalies may cause the rapid transition from the CP El Niño in 2009 to the La Niña event in 2010 via the eastward propagation of the upwelling Kelvin waves. Based on the interannual variability of upper-oceanic heat content, Ren and Jin (2013) noted that the life cycles of both CP and EP ENSO events could be explained by the recharge–discharge process associated with the thermocline feedback, which is a dominant process in the regulation of the development and phase transitions of both types of El Niño events. Therefore, the thermocline variations in the tropical Pacific may be a precursor of the evolution of the two El Niño types (Wen et al. 2014). However, Kao and Yu (2009) presented an opposing viewpoint that equatorial Pacific thermocline variations are not crucial in the development of CP El Niño events. Subsequently, Kug et al. (2009) stressed that the zonal advection of the mean SST by abnormal zonal currents plays a key role in the generation phase of the CP El Niño, whereas the thermocline feedback may be less important. Because the discharge of upper-oceanic heat content in the central equatorial Pacific is weak, the thermocline feedback may not be the key factor for the phase transition of the CP El Niño, which is rarely followed by a La Niña event (Kug et al. 2010). Yu et al. (2010) suggested that the initial establishment of the CP El Niño may be attributed to the air–sea interaction in the northeastern subtropical Pacific.

The intense argument on the feedback of thermocline to the CP El Niño is possibly due to the fuzzy structure of thermocline fluctuation. Therefore we intend to propose a new method of simple mode function decomposition, used to distinguish the dominant spatial structure of equatorial thermocline with respect to the two El Niño types (see the appendix). The dominant modes of SOTAs associated with EP and CP El Niño events have been discussed (i.e., Yu et al. 2011; Xu et al. 2012), and the current work further explores the physical attributes of the equatorial Pacific thermocline variability and the eastward propagation of ocean–atmosphere processes, which is possibly related to the CP El Niño via the mode function decomposition method.

The remainder of the paper is organized as follows. The datasets and methods are briefly introduced in section 2. Section 3 demonstrates the dominant equatorial Pacific thermocline modes revealed by the mode function decomposition method. Comparisons of the thermocline- and SST-based EP and CP El Niño events are addressed in section 4, and the role of the equatorial thermocline in the evolution of the CP El Niño is examined in section 5. Finally, a summary and discussion are presented in section 6.

2. Data and methods

a. Data

The monthly subsurface ocean temperature and wind stress are derived from a retrospective analysis of the global ocean based on the Simple Ocean Data

Assimilation (SODA, version 2.1.6) package (Carton et al. 2005). This dataset covers the global ocean with a horizontal resolution of 0.5° × 0.5° and 40 standard vertical depth levels, spanning from January 1958 to December 2008. The thermocline depth in the equatorial Pacific is defined as the depth of the 20°C isotherm (henceforth referred to as D20; Kessler 1990). The thermocline depth data from the National Centers for Environmental Prediction Global Ocean Data Assimilation System (GODAS) product (Behringer and Xue 2004) are utilized and compared with that from the SODA 2.1.6 data. Monthly SSTAs are extracted from the Hadley Centre Global Sea Ice and Sea Surface Temperature (HadISST version 1.1) analysis dataset with a horizontal resolution of 1° × 1° from 1958 to 2008 (Rayner et al. 2003). The surface heat flux datasets are derived from the Twentieth Century Reanalysis (20CR; Compo et al. 2011). A 3-month running average is conducted on all the monthly variables to remove the subseasonal variability, and the anomalies are the deviation from the seasonal mean. The study spans the period 1958–2008, and all statistical significance tests are performed using a two-tailed Student's t test.

The conventional EP El Niño is identified by the Niño-3 index, which is defined by the area-averaged SSTAs over the eastern-central equatorial Pacific region (150°–90°W, 5°S–5°N). The CP El Niño is quantified by the El Niño Modoki index (EMI; Ashok et al. 2007), which is defined as

$$\mathrm{EMI} = [\mathrm{SSTAs}]_C - 0.5[\mathrm{SSTAs}]_E - 0.5[\mathrm{SSTAs}]_W, \quad (1)$$

where the square brackets with a subscript represent the area-averaged SSTAs over the central Pacific (subscript C: 165°E–140°W, 10°S–10°N), the eastern Pacific (subscript E: 110°–70°W, 15°S–5°N), and the western Pacific (subscript W: 125°–145°E, 10°S–20°N), respectively.

b. Methods

In addition to the mode function decomposition method (seen in the appendix), a mixed layer heat budget analysis is performed to investigate the physical processes related to the CP El Niño SSTAs. The mixed-layer temperature (MLT) budget (Li et al. 2002) can be described by the following equation:

$$\frac{\partial T'}{\partial t} = -\left(u'\frac{\partial \overline{T}}{\partial x} + \overline{u}\frac{\partial T'}{\partial x} + u'\frac{\partial T'}{\partial x}\right) - \left(v'\frac{\partial \overline{T}}{\partial y} + \overline{v}\frac{\partial T'}{\partial y} + v'\frac{\partial T'}{\partial y}\right) - \left(w'\frac{\partial \overline{T}}{\partial z} + \overline{w}\frac{\partial T'}{\partial z} + w'\frac{\partial T'}{\partial z}\right) + \frac{Q'_{\mathrm{net}}}{\rho c_p H} + R, \quad (2)$$

where the bars and primes represent the climatologic mean variables and the anomaly departure from the climatological mean, respectively. The quantities T, u, v, and w indicate the oceanic temperature, and the zonal, meridional, and vertical velocities averaged over the mixed layer, respectively. The first three groups of terms on the right-hand side of the equation denote the oceanic heat advection in the zonal, meridional, and vertical directions, respectively. The final term is the surface heat flux term, and a positive value indicates heat flux into the ocean. The, Q_{net} is the summation of the net downward shortwave radiation absorbed in the mixed layer (Q_{sw}), net downward surface longwave radiation, and surface latent and sensible heat fluxes; R represents the residual term, ρ is the seawater mean density, and C_p is the heat capacity of seawater under constant pressure.

Following Wang et al. (2012) and Chen et al. (2016), the mixed layer depth (H) is defined as the depth where the water temperature is 0.8°C lower than the surface value. All budget terms in Eq. (2) are defined as averaged over the depth of the mixed layer. Considering the shortwave penetration below the mixed layer, the Q_{sw} absorbed in the mixed layer can be written as (Wang et al. 2012)

$$Q_{\mathrm{sw}} = Q_{\mathrm{surf}} - 0.47Q_{\mathrm{surf}}e^{-0.04H}, \quad (3)$$

where Q_{surf} is the net downward surface shortwave radiation.

3. Equatorial Pacific thermocline

We first present the climatological D20 in the global equatorial ocean (Fig. 1a). It is observed that the equatorial thermocline slopes down westward in both the Pacific and Atlantic Oceans, but it slopes slightly up westward in the Indian Ocean. The steepest slope of the equatorial thermocline is located in the Pacific Ocean. These basic structures of the equatorial thermocline are primarily ascribed to the prevailing surface wind in annual-mean climatology: strong trade easterlies over the equatorial Pacific and Atlantic basins, but weak westerlies over the Indian Ocean. In addition, the equatorial thermocline is steeper in the southern equatorial Pacific, exhibiting a slight asymmetry to the equator, which is likely caused by the fluctuations of the two subtropical gyres in the Northern and Southern Hemispheres (Wyrtki 1989). The temporal evolution of the equatorial Pacific basin mean (5°S–5°N, 130°E–80°W) D20 is shown in Fig. 1b. It can be clearly seen that the depth of the equatorial thermocline in the Pacific Ocean varies significantly on interannual and decadal time scales. Specifically, the D20 in the equatorial Pacific became shallower after 1980; in fact, the mean D20 decreased from 134.0 m before 1980 to 126.2 m after 1980. This change may be attributed to the persistence of

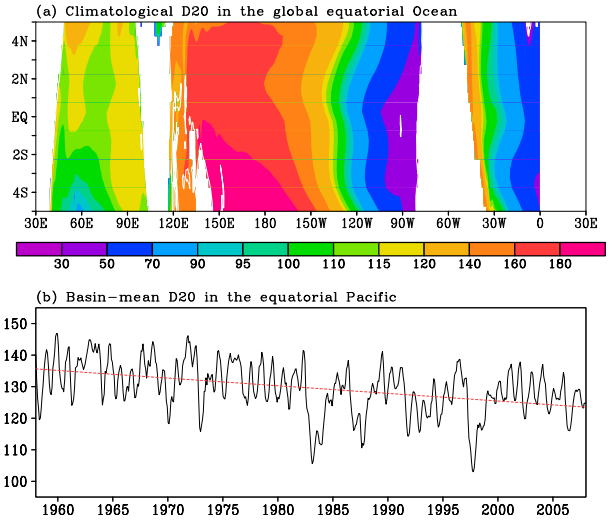

FIG. 1. (a) The climatological D20 (m) in the global equatorial ocean. (b) Time evolution of the basin-mean (5°S–5°N, 130°E–80°W) D20 in the equatorial Pacific (black solid line, m) and its corresponding trend (red dashed line).

La Niña–like background state in the tropics, with cold (warm) SSTAs appearing in the eastern (western) equatorial Pacific over the past three decades (Kosaka and Xie 2013; Xiang et al. 2013; Chung and Li 2013). To further extract the leading modes of the interannual equatorial Pacific thermocline variability, the mode function decomposition method is applied using the SODA 2.1.6 dataset after its linear trend has been removed.

a. Spatial patterns of the decomposed modes

According to the mode function decomposition method, the climate-mean thermocline structure in the equatorial Pacific can be approximately represented by the first three modes: modes 0, 1, and 2. Of these, mode 0 is the lowest-order mode of the thermocline, representing the anomalous mean thermocline depth; it is not discussed hereafter. Figure 2a shows the fractional variance explained by the leading eight modes of the equatorial Pacific thermocline and their corresponding errors. The mode expansion rapidly converges, and the first mode (M1), second mode (M2), and third mode (M3) account for 24.8%, 11.5%, and 7.8% of the total variance, respectively. Their errors do not overlap each other, suggesting that the first three modes are well separated, as per the rule of thumb of North et al. (1982). In contrast, the amplitudes of the higher-order modes generally become much smaller (not shown), and the corresponding error bars related to the higher modes (i.e., M4, M5, and M6) overlap each other (Fig. 2a), indicating that the higher-order modes are not entirely independent. Therefore, the first three modes are independent of each other, and M1 and M2 may describe the main features of thermocline fluctuations, with respective to the two pivotal types of El Niño events. M1 and M2 show the capability to catch the structure of the equatorial Pacific thermocline during the mature phase of EP and CP El Niño events, which is supported by the equatorial Pacific D20 anomaly and the reconstructions based on mode function decomposition $[\Sigma a_i(t)f_i(x)]$ in boreal winter [December–February (DJF)].

Following Yu et al. (2012), we select five CP El Niño events (1958/59, 1968/69, 1977/78, 1994/95, and 2004/05) and five EP El Niño events (1972/73, 1976/77, 1982/83, 1997/98, and 2006/07) during 1958–2008. In the case of EP El Niño events, both the observed equatorial Pacific D20 anomaly and the M1 exhibit a basinwide zonally tilted pattern, with shoaling in the western Pacific and deepening in the eastern Pacific (Fig. 2b); this pattern corresponds to the zonal dipolar SSTAs with warming SSTAs in the eastern–central equatorial Pacific and cooling SSTAs in the western tropical Pacific. The reconstructions from the leading six modes may clearly describe the essential zonal structure of the equatorial Pacific thermocline anomaly in the EP El Niño events, but the change contributed by the higher than M1 modes is limited (Fig. 2b). Therefore, the M1 can be regarded as the dominant component in the mature phase of EP El Niño events.

In the case of CP El Niño events, however, an essential structure of the V shape is observed in the reconstructed thermocline depth anomaly by the leading six modes; the deepest D20 anomalies appear in the central equatorial Pacific with relatively shallow anomalies in both the western and eastern equatorial Pacific (Fig. 2c). Note that the sum of the first two modes is mostly consistent with the observations, and the modification of the reconstructions due to modes higher than M2 makes only a small incremental contribution. As a result, we can regard the M2 as the most important mode in the mature phase of CP El Niño events.

b. Temporal evolution of M1 and M2

The EP and CP El Niño has been measured by the indices, respectively defined by the Niño-3 index and the EMI (Niño-3/EMI; Ashok et al. 2007), the EP and CP index (EPI/CPI, Kao and Yu 2009), and the warm-pool (WP) and cold-tongue (CT) index (CTI/WPI; Ren and Jin 2011). The normalized time series of the M1 amplitude (hereafter referred to as the M1 index) can well resemble the remarkable interannual variability shown by the indices of CTI, EPI, and Niño-3 (Fig. 3a), with the maximum correlation of +0.85, +0.47, and +0.91 with CTI, EPI, and Niño-3, respectively at 0 lag. The strongest EP El Niño events in 1982/83 and 1997/98 can be easily recognized as the two maxima in the M1 index.

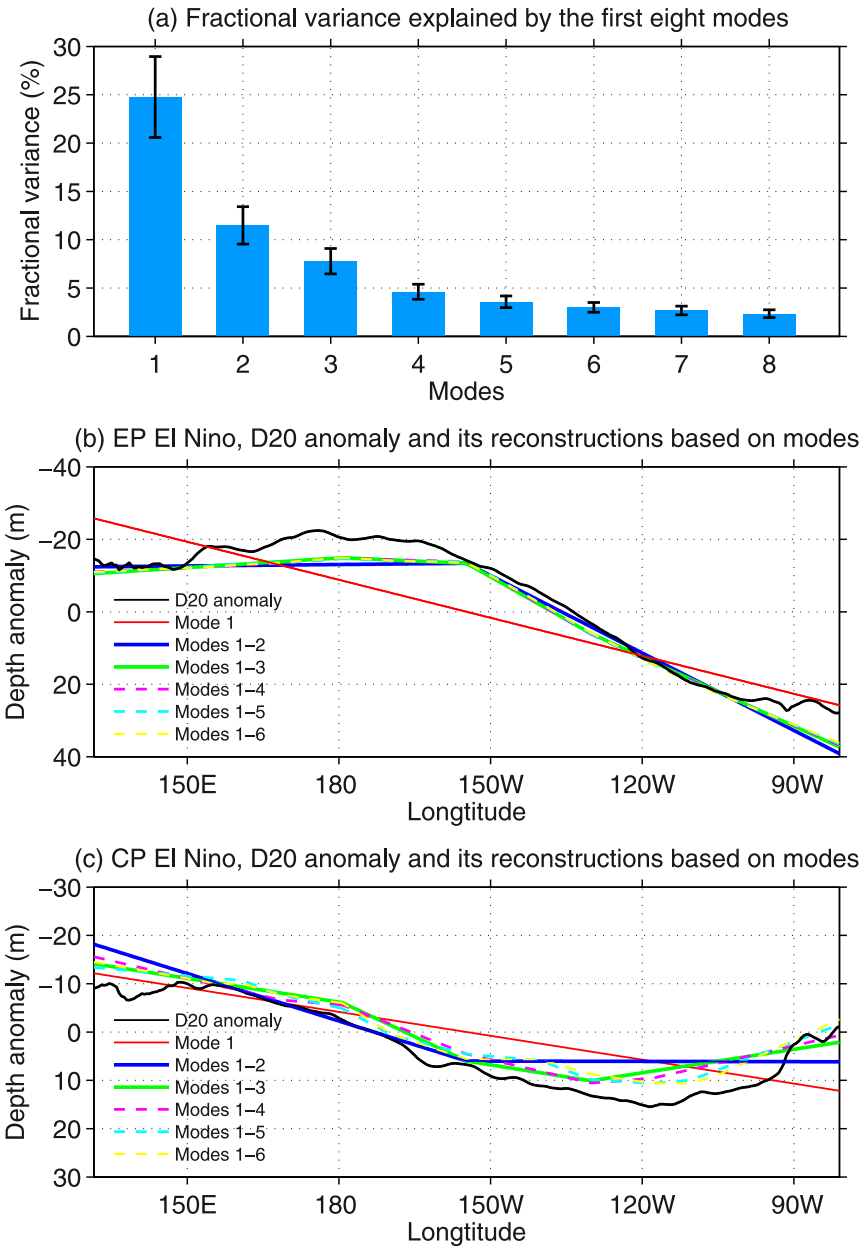

FIG. 2. (a) Fractional variance explained by the first eight mode decompositions of the equatorial Pacific D20 anomaly. The error bars indicate the corresponding errors statistically significant at the 95% confidence level based on the rule of thumb of North et al. (1982). (b) Ensemble mean for the DJF-mean equatorial Pacific D20 anomaly and the accumulated sum of modes from the first mode to the sixth mode associated with the EP El Niño events (1972/73, 1976/77, 1982/83, 1997/98, and 2006/07). (c) As in (b), but for the CP El Niño events (1958/59, 1968/69, 1977/78, 1994/95, and 2004/05). Following the tradition in oceanography, in (b) and (c) the depth anomaly is positive in the downward direction.

Similarly, the time series of the M2 amplitude (hereafter referred to as the M2 index) reflect the time evolutions of the EMI, CPI, and WPI, with simultaneous correlation coefficients of +0.68, +0.53, and +0.52, respectively, exceeding the 95% confidence level. The typical CP El Niño of the 1958/59, 1968/69, 1977/78, and 2004/05 events can be clearly identified by the M2 index (Fig. 3b). Notably, the M2 index reaches the maximum positive correlation with the EMI, WPI, and CPI when it leads by one to three months (not shown), implying that

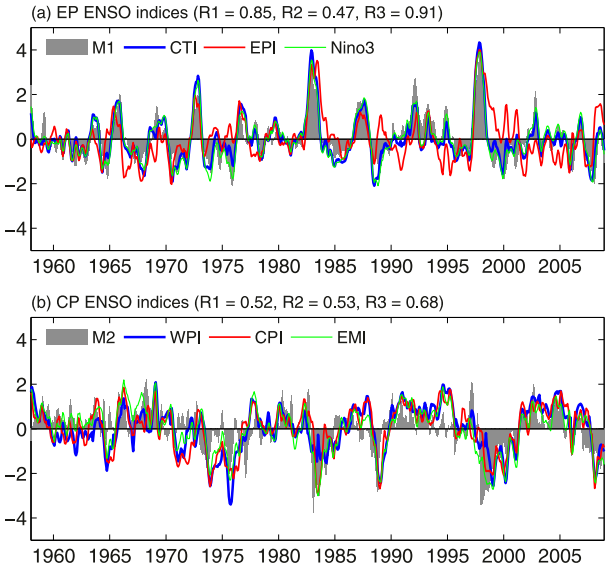

FIG. 3. (a) Normalized time evolution of the first mode (M1) index of the D20 in the equatorial Pacific (gray shading), CTI (blue line), EPI (red line), and Niño-3 index (green line) during the period 1958–2008. (b) As in (a), but for the second mode (M2) index of the equatorial Pacific D20 (gray shading), WPI (blue line), CPI (red line), and EMI (green line). Quantities R1, R2, and R3 shown in the upper (lower) panel are the simultaneous correlation coefficients between M1 (M2) and CTI, EPI, and Niño-3 (WPI, CPI, and EMI), respectively.

the CP El Niño–related signals in the SOTAs appear earlier than the counterparts for the SSTAs. Moreover, the skewness coefficient is 0.88 for M1 and −0.96 for M2, indicating the preference of the EP type for strong El Niño events and the CP type for strong La Niña events; this finding is consistent with previous studies (Kao and Yu 2009; Yu et al. 2010; Xu et al. 2012, 2013; Li et al. 2015).

Because of the highly correlations between the EP El Niño and CP El Niño index (in addition to a +0.25 correlation coefficient between the Niño-3 and EMI indices), we cannot accurately distinguish the type of El Niño events based on a single index (i.e., the Niño-3 or EMI). In contrast, the correlation between the M1 and M2 indices is close to 0 (only +0.09) at 0 lag, which shows an advantage in classifying the type of El Niño. It should be noted that the M2 index is significantly correlated with the M1 index when the M1 index lags by two to three months (not shown), suggesting that the M2 mode may be involved in the recharge process (Jin 1997) before the amplitude of M1 grows. The correlation reaches the peak negative phase when the M1 index leads the M2 index by up to 9 months (not shown); thus, M2 may be involved in the discharge process (Jin 1997) after M1 matures. The M1 and M2 indices are also evaluated using the SODA and GODAS datasets. For the overlap period 1980–2008, the M1 and M2 indices for the GODAS and SODA dataset show consistent variability; the correlation coefficients of the two indices between these two datasets are +0.98 and +0.95, statistically significant at the 95% confidence level (not shown).

Based on the criterion of National Oceanic and Atmospheric Administration (NOAA), an El Niño event is defined by the oceanic Niño index (ONI) when it is greater than or equal to 0.5°C for at least five consecutive overlapping seasons. Therefore, 17 El Niño events can be identified by the four different methods during the period 1958–2008 (Table 1). In present study, the type of CP (EP) El Niño is defined to be dominant when the DJF-averaged values of M2, WPI, CPI, and EMI are greater (less) than those of the EP El Niño indices (M1, CTI, EPI, and Niño-3). It is found that there are nine El Niño events are classified as the same type by all methods, including five (1972/73, 1976/77, 1982/83, 1997/98, and 2006/07) EP-type El Niño events and four (1958/59, 1968/69, 1977/78, and 2004/05) CP-type El Niño events (hereafter referred to as pure CP El Niño events). But the remained eight events are classified into two different types by the M1/M2 and the EPI/CPI methods. In contrast, the M1/M2, CTI/WPI, and Niño-3/EMI indices reach a general consensus on identifying the EP El Niño types (i.e., 1965/66, 1969/70, 1986/87, and 1991/92). These results suggest that the thermocline-based El Niño indices are not only able to describe the equatorial Pacific thermocline variation but also are also useful for effectively identifying both EP and CP El Niño events.

Empirical orthogonal function (EOF) analysis has been popularly utilized to examine the dominant modes in the ocean and atmosphere fields. To reveal the stability of the EOF mode with time, we applied the EOF to the equatorial Pacific thermocline of SODA during 1958–2008, 1958–74, 1975–91, and 1992–2008, respectively. Figure 4 depicts the first two leading modes (EOF1 and EOF2) and their corresponding principal components (PC1 and PC2). The EOF1 displays a basinwide east–west-tilted thermocline anomaly, with shoaling in the western Pacific and deepening in the eastern Pacific (Fig. 4a), and PC1 matches well with the M1 index, with a high correlation coefficient of +0.95 during 1958–2008. Moreover, the EOF2 mode exhibits a V-shaped thermocline, with the deepest D20 anomalies in the central and relatively shallow D20 anomalies in both the western and eastern equatorial Pacific (Fig. 4b); the PC2 is significantly correlated with M2 index, with correlation coefficient of +0.68. Therefore, the EOF analysis resembles the dominant modes from the mode function decomposition analysis. However, the leading EOF modes exhibit striking differences, and they are

TABLE 1. The El Niño events during 1958–2008, identified by the NOAA's oceanic Niño index (ONI) and the corresponding types determined by the method of M1/M2, CTI/WP, EPI/CPI, and Niño-3/EMI, respectively. The boldface and italic El Niño events indicate that all four methods identify the event as the same type.

		Type			
No.	El Niño years	M1/M2 index	CTI/WPI	EPI/CPI	Niño-3/EMI
1	***1958/59***	***CP***	***CP***	***CP***	***CP***
2	1963/64	EP	EP	CP	CP
3	1965/66	EP	EP	CP	EP
4	***1968/69***	***CP***	***CP***	***CP***	***CP***
5	1969/70	EP	EP	CP	EP
6	***1972/73***	***EP***	***EP***	***EP***	***EP***
7	***1976/77***	***EP***	***EP***	***EP***	***EP***
8	***1977/78***	***CP***	***CP***	***CP***	***CP***
9	***1982/83***	***EP***	***EP***	***EP***	***EP***
10	1986/87	EP	EP	CP	EP
11	1987/88	EP	CP	CP	EP
12	1991/92	EP	EP	CP	EP
13	1994/95	EP	CP	CP	CP
14	***1997/98***	***EP***	***EP***	***EP***	***EP***
15	2002/03	EP	CP	CP	EP
16	***2004/05***	***CP***	***CP***	***CP***	***CP***
17	***2006/07***	***EP***	***EP***	***EP***	***EP***

very sensitive to the selected periods (Fig. 4). For example, the EOF2 is characterized by a basinwide east–west-tilted thermocline anomalies during 1975–91 (Fig. 4b), but it failed to capture the V-shaped thermocline depicted by M2 (Fig. A1). Moreover, the PC2s exhibit significant differences among the study periods (Fig. 4d), although the PC1s show little change (Fig. 4c). Because the M1 and M2 modes are time independent and their corresponding amplitudes are comparable in any study period, the mode function decomposition method is more stable and able to capture the essential feature of the equatorial thermocline compared to the EOF analysis

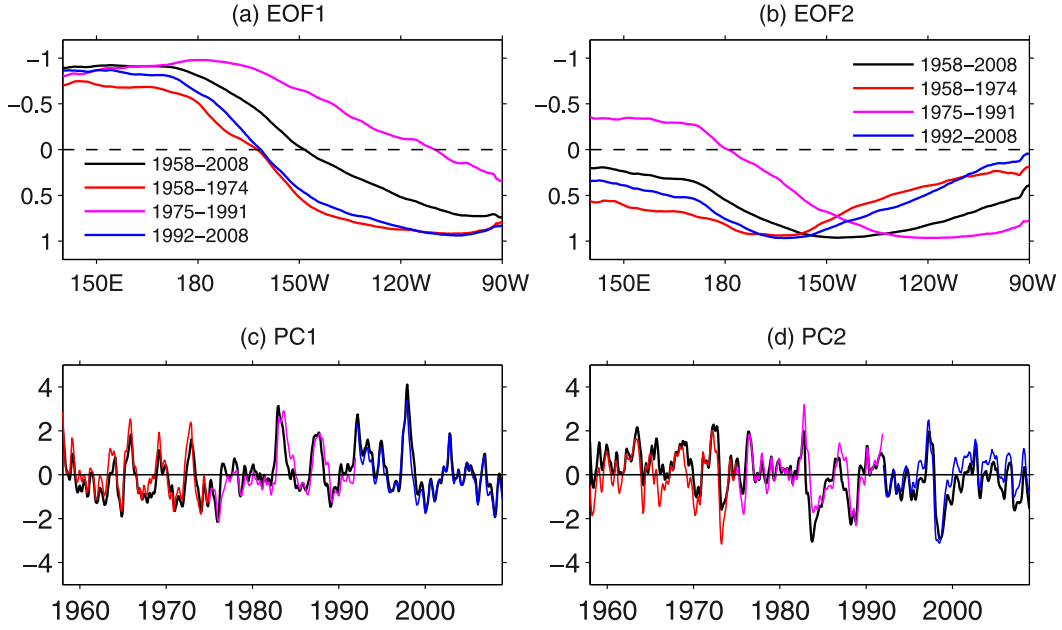

FIG. 4. The (a) first and (b) second leading EOF modes (EOF1 and EOF2) of the equatorial Pacific thermocline over the periods 1958–2008 (black line), 1958–74 (red line), 1975–91 (magenta line), and 1992–2008 (blue line) based on the SODA dataset and the corresponding (c) first and (d) second principal components (PC1 and PC2). Following the tradition in oceanography, in (a) and (b) the depth anomaly is positive in the downward direction.

method. Therefore, the M1 and M2 indices provide us with benchmarks to distinguish the EP and CP El Niño, respectively.

4. Comparison of thermocline and SST-related El Niño events

a. *Interannual and decadal time scales*

More discussions have focused on the different temporal features of CP and EP El Niño events by previous studies (i.e., Weng et al. 2007; Yeh et al. 2009; Xu et al. 2012, 2014; Wang and Wang 2014). The CP El Niño events include strong interannual and decadal signals, whereas the EP El Niño events are predominated by strong interannual variability. The wavelet power spectra and global power spectra of the M1/M2 index suggest that the EP El Niño exhibits a significant quasi-quadrennial variability (Fig. 5a), but the oscillations of the CP El Niño show a clear quasi-biennial band (Fig. 5b). This contrast in periodicity between the two types of El Niño events is amplified in the thermocline-based El Niño indices, consistent with the results of Yu et al. (2011). In addition, the M2 index exhibits a quasi-quadrennial band and an 8–16-yr band, with respect to the CP El Niño (Fig. 5b). The decadal oscillations in the M2 index become more remarkable after the 1980s, suggesting a transition of higher-frequency CP El Niño in recent decades (Kug et al. 2009; Yeh et al. 2009; Lee and McPhaden 2010; Xu et al. 2012, 2014). Both M1 and M2 exhibit significant interannual variability, whereas the higher modes (i.e., M3 and M4) are only significant for less than 1-yr oscillations (figure not shown). Compared with the EP and CP El Niño events defined by Kao and Yu (2009), M1 and M2 show stronger amplitude on interannual time scale; therefore, M1 and M2 could potentially be more effective in capturing the interannual variations of the EP and CP El Niño events.

b. *Seasonal evolution*

In contrast to the SST-based indices, M1 and M2 also show a good performance in describing the seasonal evolution of EP and CP El Niño events, which can be supported by the lag–lead correlations of M1 and M2 with the equatorial D20 anomalies, averaged between 5°S and 5°N (Fig. 6). Note that the higher correlations for the two El Niño types appear at 0 lag, corresponding to their peak phases. Therefore, the zonal gradient of the equatorial Pacific thermocline is the most prominent in the mature phase of two types El Niño events, regardless of which index is used.

During the mature phase of EP El Niño, the Niño-3 index-correlated D20 anomalies exhibit a significant dipolar pattern over the equatorial Pacific, which can be tracked back to at least two seasons before peak phase (Fig. 6a). Specifically, the significant and positive D20 anomalies are first observed from 180° to 80°W approximately one year before the peak phase. Subsequently, the positive D20 anomalies are gradually enhanced and move eastward to the eastern equatorial Pacific, where the thermocline deepens. Meanwhile, the D20 anomalies reach their maximum over the western Pacific and lead the shallower thermocline anomalies six months later (Fig. 6a). The evolution of the D20 anomaly identified by the M1 index resembles the EP El Niño cycle, except with larger amplitude (Fig. 6c). In fact, the leading D20 anomalies occur in the eastern equatorial Pacific, suggesting the important impact of SOTAs on the following EP El Niño events. The SOTAs gradually propagate eastward along the equatorial Pacific thermocline to the eastern equatorial Pacific during the developing EP El Niño. Consequently, they cause the local warming in the SSTAs via a thermocline feedback (Jin 1997).

However, the evolution of the D20 anomalies associated with different indices is more prominent in CP El Niño events. For instance, there is no clear zonal eastward propagation of the equatorial SOTAs observed in the EMI-defined CP El Niño events (Fig. 6b). Meanwhile, the positive D20 anomalies near the central equatorial Pacific are weak in the mature phase (Fig. 6b), and the monopole peaking structure of the D20 anomalies at 0 lag is not significant in these cases. In contrast, in the cases of the CP Niño events defined by the M2 index, the enhanced positive D20 anomalies first occur in the western equatorial Pacific (120°–170°E), and they gradually strengthen and propagate eastward to the central equatorial Pacific approximately one year before the peak phase (Fig. 6d). The monopole structure of D20 anomalies around the date line becomes the most remarkable in the equatorial Pacific when the CP El Niño reaches its peak phase (Fig. 6d). The lag–lead correlations of the SSTAs averaged between 5°S and 5°N for the thermocline- and SST-based indices both show that the SSTAs signals with respect to the zonal eastward propagation are not remarkable (Fig. 7), and these results are quite different from that for the D20 anomalies (Fig. 6). During the life cycle of CP El Niño, the maximum SST warming appears in the central equatorial Pacific three to four months later than that associated with SOTAs (Figs. 6d and 7d). The warming SSTAs reach their peak in boreal winter (Yu et al. 2012; Xu et al. 2017), but the SOTAs reach the peak in autumn [September–November (SON)], characterized by the monopole peaking of SOTAs around the central equatorial Pacific. These distinct zonal eastward propagations between the thermocline and SST field anomalies can be

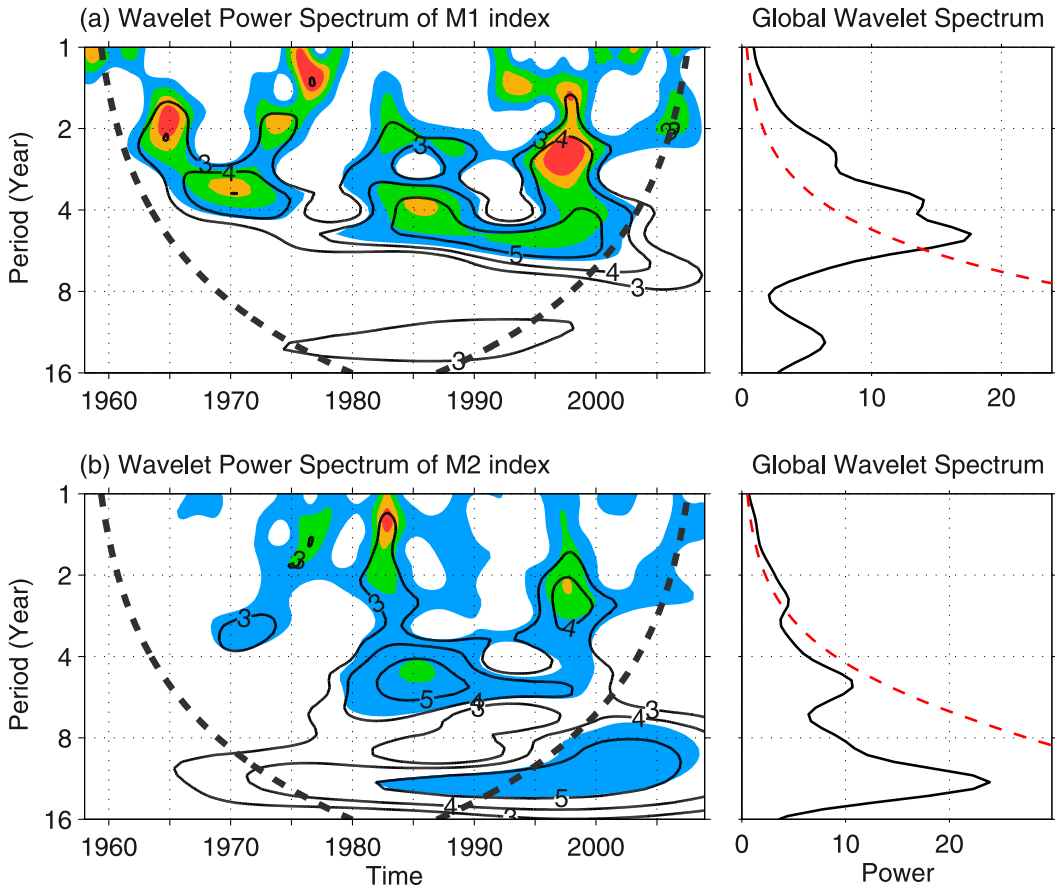

FIG. 5. Wavelet analysis and the global power spectrum of the monthly (a) M1 and (b) M2 indices. The colored areas indicate statistical significance at the 95% confidence level against red noise processes, and the regions of dashed black lines on either end indicate the "cone of influence," where edge effects become important. In the right panels, the solid black line is the global wavelet power spectrum, and the dashed red line shows its significance at the 95% confidence level.

well observed in Figs. 6 and 7. This implies that the M2 index might be more efficient in reflecting the zonal eastward propagation of SOTAs during the developing phase of CP El Niño event.

5. Role of the equatorial thermocline during CP El Niño events

a. Ocean–atmosphere coupled processes

The ocean–atmosphere coupled processes for the CP El Niño events can be clearly observed in the lead–lag M2 index-regressed SOTAs (upper 400 m), SSTAs, and wind stress anomalies in the tropical Pacific (Figs. 8 and 9). Note that the most remarkable tripolar SOTAs pattern is treated as the SOTA peak of the CP El Niño at 0 lag (Fig. 8g). A zonal SOTA dipole is observed one year before the SOTAs peak in the equatorial Pacific, where a substantial warming and a robust cooling prevail in the western and eastern equatorial Pacific, respectively (Fig. 8a). Horizontally, there is a weak increase in SSTAs near the center of 8°N, 160°E, but a strong decrease in the eastern Pacific (Fig. 9a). The easterly anomalies prevail over the equatorial Pacific, accompanied by the emerging anomalous westerlies in the western Pacific (Figs. 9b–e). The anomalous westerlies may stimulate the downwelling equatorial Kelvin waves and deepen the thermocline from the western to the central equatorial Pacific. As a subsurface ocean response, substantial increases of SOTAs in the western Pacific gradually develop and propagate eastward along the equatorial Pacific thermocline (Figs. 8b–e), together with the eastward extension of increasing SSTAs (Figs. 9b–e). These features of the SOTAs evolution are remarkably different from the EMI-regressed SOTAs during the developing stage of CP El Niño. For instance, the center of positive SOTAs depicted by the EMI is confined near the date line, but no significant eastward

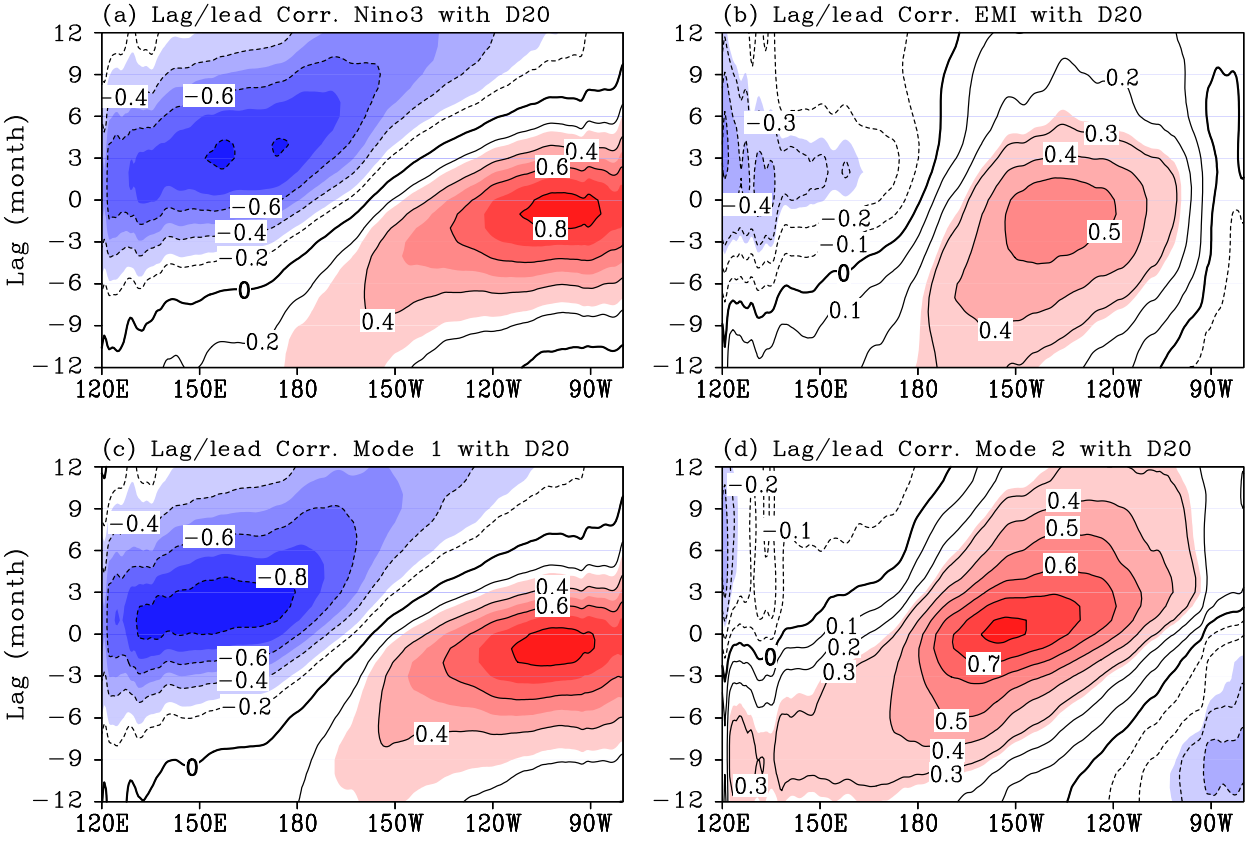

FIG. 6. Lag–lead correlations of the (a) Niño-3 index, (b) EMI, (c) M1, and (d) M2 time series with the D20 anomalies averaged between 5°S and 5°N during the period 1958–2008. Negative (positive) lag values on the *y* axis indicate D20 anomalies leading (lagging) the indices, and colored regions are statistically significant at the 90% confidence level based on the Student's *t* test.

propagation is observed in the increasing SOTAs (Ashok et al. 2007; see their Fig. 8).

The SOTAs develop slowly during 4–12 months leading periods in the region between 5° and 10°N at upper 100 m in the western Pacific (not shown), similar to the results near the equator (Figs. 8a–e). However, the enhancement is obvious for the local SSTAs around 8°N (Figs. 9a–e), different from the strengthening positive SOTAs along the thermocline. Therefore there is no close coupling between SSTAs and SOTAs in the western Pacific at this point. Moreover, there is no clear zonal eastward propagation of SSTAs during the CP El Niño events (Fig. 7d). These results imply that the enhanced SSTAs in the western Pacific may increase and extend eastward into the central equatorial Pacific due to the local air–sea interactions, such as the wind–evaporation–SST (WES) feedback (Xie and Philander 1994) and the cloud-radiation effect (Li et al. 2000). In addition, significant positive SSTAs, possibly induced by the extratropical atmosphere (Yu et al. 2010; Yu and Kim 2011), appear off Baja California approximately eight months before the CP El Niño SOTAs peak (Fig. 9c). Through the WES feedback, the warming SSTAs enhance and persist in the northeastern subtropical Pacific, and extend southwestward to the tropics six months later (Figs. 9d–f). Subsequently, the eastward intrusion of anomalous equatorial westerlies reaches 150°W, the enhanced SSTAs in northeastern subtropical Pacific extend southwestward into the tropics (Fig. 9g), where it merges with the increased SSTAs from the western equatorial Pacific (Yu and Kim 2011).

The upper-level SOTAs start to decrease, creating a weak cold center in the equatorial western Pacific two months before the SOTAs peak (Fig. 8f). Correspondingly, the significant negative SSTAs in the western equatorial Pacific are located west of 140°E (Fig. 9f). This is followed by a zonal tripolar in the SOTAs over equatorial Pacific, where the robust positive SOTAs are located in the central equatorial Pacific, along with the nonsignificant weak negative SOTAs located in both the western and eastern equatorial Pacific (Fig. 8g). Meanwhile, the robust warming center of SOTAs in the central equatorial Pacific peaks with the arrival of eastward downwelling equatorial Kelvin waves in the central

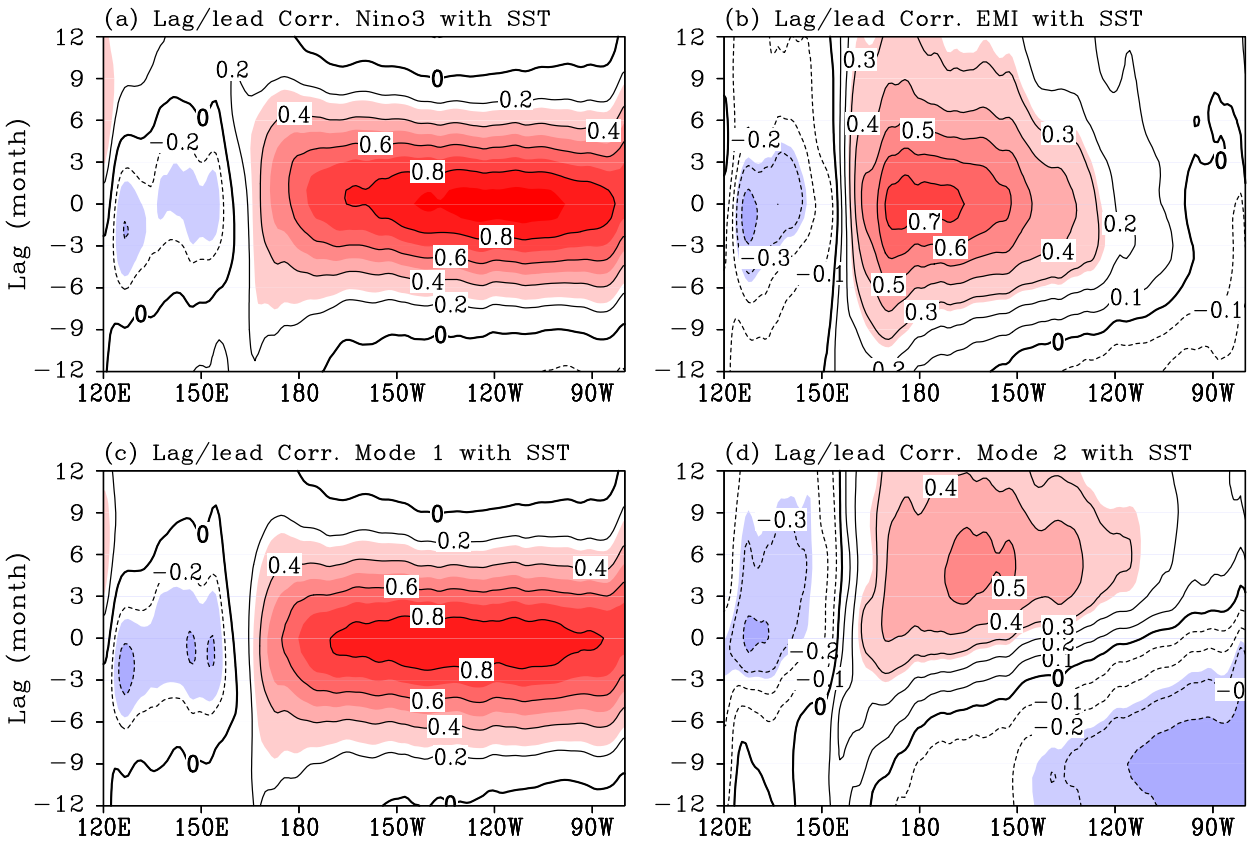

FIG. 7. As in Fig. 6, but for the SSTAs.

equatorial Pacific. The significant positive SOTAs in the upper 50 m are further strengthened after the SOTAs peak, and gradually expand upward and eastward to 120°W (Figs. 8h–j). Accordingly, the increased SST in the central tropical Pacific continues to develop, and extend eastward to reach its maximum (>+0.5°C) at approximately four to six months after the SOTAs peak (Figs. 9i, j), indicating that the peak of warming SSTAs appears 4–6 months later after their counterpart of SOTAs. Such feedback via the thermocline after the SOTAs peak can be explained by the recharge–discharge oscillator theory (Jin 1997). Therefore, the air–sea interactions may determine the establishment and initial development of the CP El Niño, but the thermocline feedback plays a vital role for its further development.

b. Heat budget analysis

Based on Eq. (2), we calculated the tendencies of the MLT anomaly heat budget terms averaged over the central equatorial Pacific (5°S–5°N, 180°–120°W) and presented the composite results one season before and after the SOTAs peak (Fig. 10). Note that the boreal autumn and winter is defined as the season before and after the SOTAs peak, respectively.

The increase of SSTAs is mainly contributed by the three-dimensional temperature advection terms, while the heat flux anomalies tend to dampen the SSTAs. The summation of the advection terms and the surface heat flux term approximates the observed MLT tendency between the two seasons before and after the SOTAs peak, implying that the mixed layer temperature budget analysis is approximately balanced, although the surface heat fluxes and oceanic subgrid processes are uncertain. The total ocean advection term has only minor differences between the two periods, although significant differences are observed in the horizontal and vertical temperature advection terms (Fig. 10). Before the SOTAs peak, the zonal and the vertical advections have no significant differences; their corresponding difference is smaller than the composited standard errors (Fig. 10). Thus, it is too difficult to distinguish which advection term is more important in terms of the growth rate. After the SOTAs peak, however, there are distinct differences between these two terms. The zonal temperature advection becomes weaker but the vertical counterpart becomes much larger, suggesting that the latter plays a dominant role in the subsequent warming peak of SSTAs. It is noted that the meridional advection is also

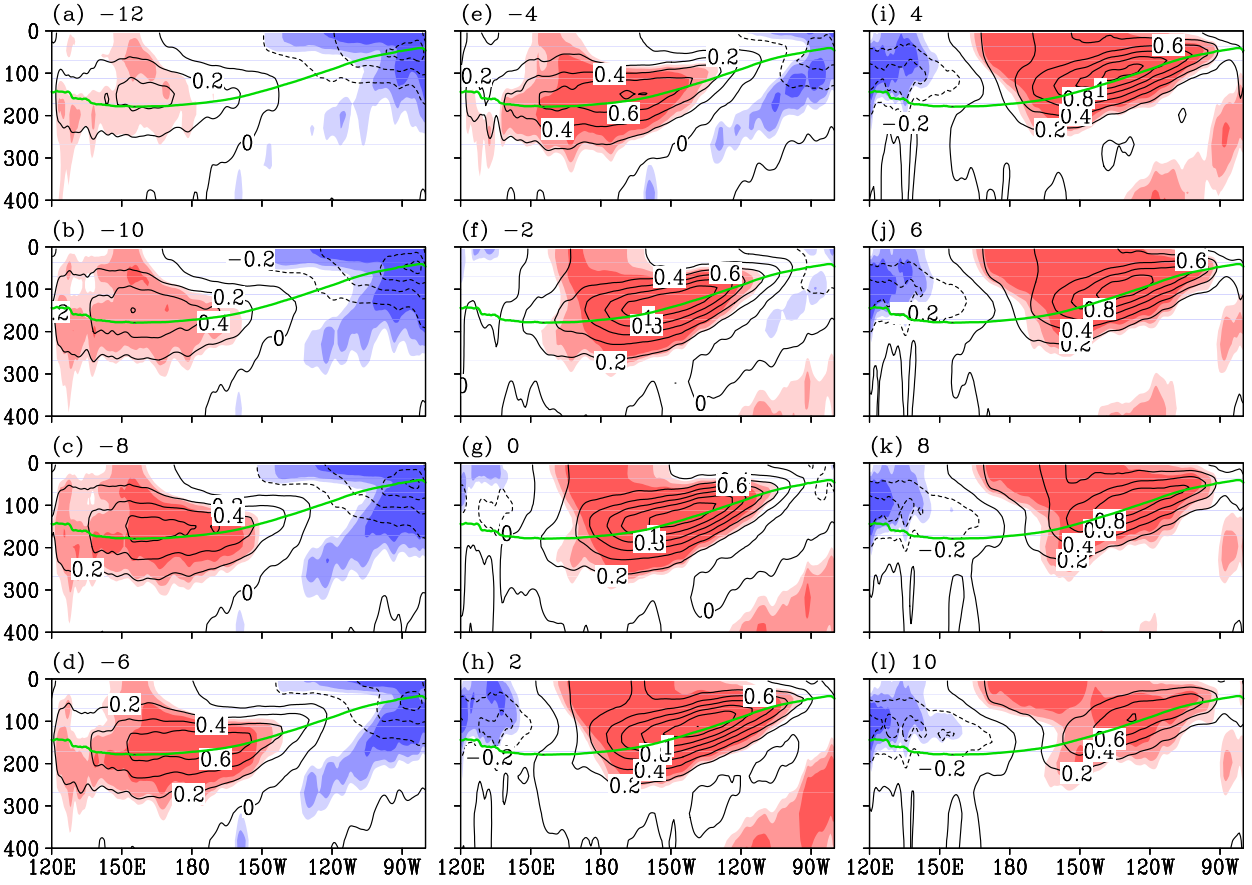

FIG. 8. Lag–lead regressions of the M2 index onto SOTAs (°C) averaged between 5°S and 5°N. Colored regions are statistically significant at the 90% confidence level based on the Student's *t* test. Negative (positive) numbers above each panel indicate the number of months by which the SOTAs lead (lag) the M2 index. The green lines are the 20°C isotherm.

relatively large during the two periods, but this term mainly contributes to the expanding of SSTAs away from the equator according to Kang and Kug (2002).

For the CP El Niño events, the SST tendency is mainly coming from the zonal advection of the mean temperature by the zonal current anomaly ($u'\partial\overline{T}/\partial x$) and the vertical advection of the anomalous temperature by the mean upwelling ($\overline{w}\partial T'/\partial z$) (Kug et al. 2009; Ren and Jin 2013; Su et al. 2014), which is related to the so-called zonal advective (ZA) and thermocline (TH) feedbacks, respectively. To fully understand the SST tendency in the cases of pure CP El Niño events, we examine the composite MLT tendency and ZA and TH feedbacks across the entire equatorial Pacific (Fig. 11). The warming tendency of the MLT is observed in the equatorial Pacific east of 160°E from June [J(0)] to the following January [J(1)], with the two strongest positive SST centers positioned at 100°W in September [S(0)] and at 180° in December [D(0)] (Fig. 11a). This warming tendency prevails until the following March [M(1)], which implies that the warming SSTAs in the central tropical Pacific continue to develop and extend eastward before they reach their maximum three months after the SOTAs peak; this is consistent with the results shown in Figs. 8 and 9. In the central equatorial Pacific (160°E–150°W), the ZA term is in phase with the observed SST tendency from J(0) to D(0), and its maximum magnitude (0.1°C month^{-1}) is comparable to the observed MLT tendency (Fig. 11b). Such a result suggests the ZA feedback plays a crucial role in the developing and mature phases of pure CP El Niño events.

The TH term with respect to thermocline feedback increases after the SOTAs peak, with the maximum warming tendency occurring in the following February [F(1)] (Fig. 11c), despite the fact that it is relatively small. This finding suggests that the thermocline feedback largely contributes to the CP SSTAs growth after the SOTAs peak and may result in the peak of warming SSTAs. In addition, both the SOTAs (Figs. 8a–g) and SSTAs (Figs. 9a–g) change from negative to positive anomalies in the eastern equatorial Pacific during the life cycle of CP El Niño events. This process is associated

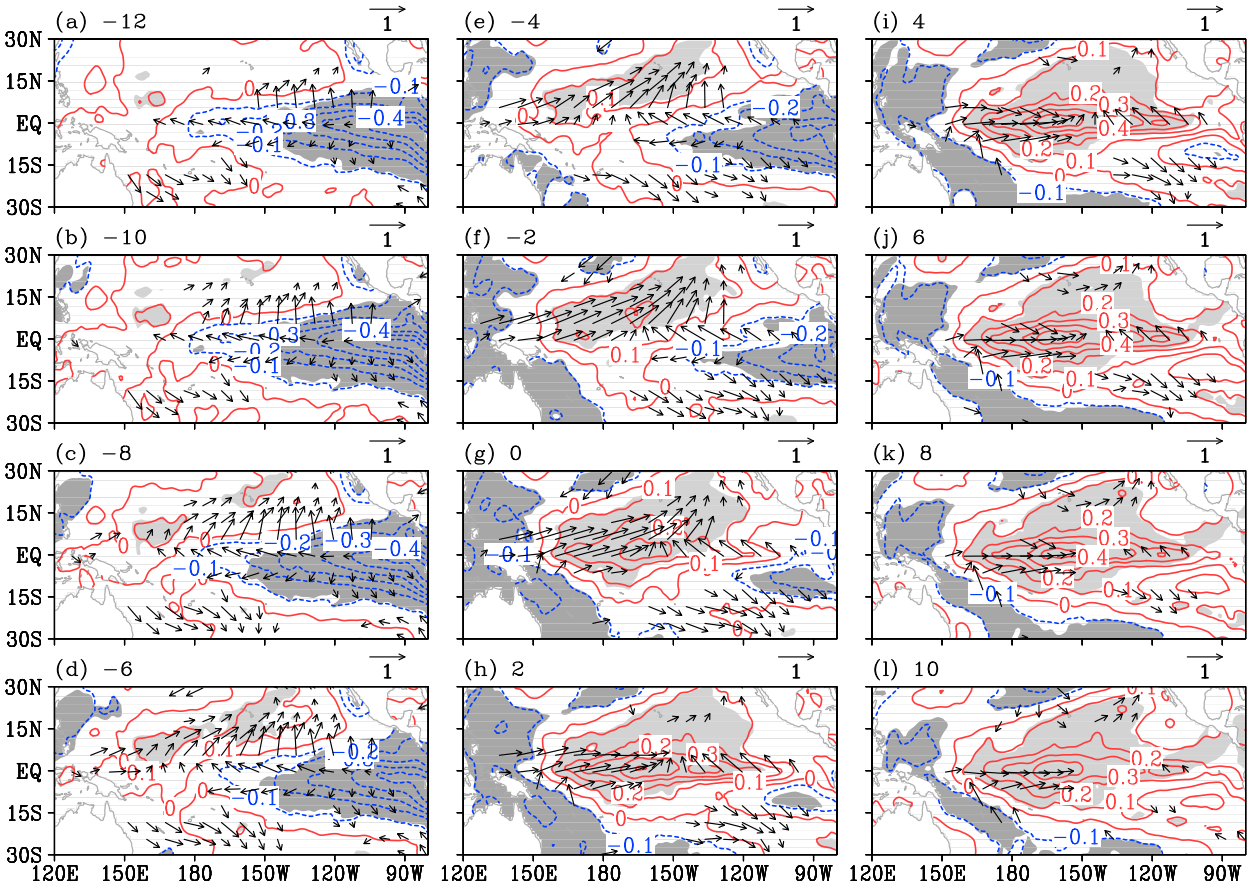

FIG. 9. Lag–lead regressions of the M2 index with SSTAs (contours, °C) and wind stress anomalies (vectors, 0.01 N m^{-2}) over the tropical Pacific. The black wind vectors and the shaded regions indicate the wind stress anomalies and the SSTAs, respectively, above the 90% confidence level based on Student's *t* test: light shading represents significant positive correlations, and dark shading indicates negative correlations. Negative (positive) numbers above each panel indicate the number of months by which the anomaly distribution fields lead (lag) the M2 index.

with the eastward retreat of the decreased easterlies (Figs. 9a–g), mainly caused by the powerful thermocline feedback (Fig. 11c). These analyses demonstrate that the ZA feedback determines the establishment and development stage of CP El Niño events, but the thermocline feedback is vital for its further development. Therefore the precursor fluctuations in the equatorial thermocline can be regarded as an indicator of CP El Niño events, due to their adjustment occurring 4–6 months ahead of the SSTAs peak. Of course, the increasing SSTAs and surface wind anomalies in the subtropical Pacific are also precursors to the occurrence of CP El Niño events.

6. Summary and discussion

In the present study, we propose a mode function decomposition method and use it to distinguish the dominant mode in the equatorial thermocline fluctuations, with respect to the EP and CP El Niño events. The first mode (M1) represents a basinwide zonally tilted thermocline anomaly with shoaling in the western Pacific and deepening in the eastern Pacific. However, the second mode (M2) depicts the V-shaped thermocline anomaly in the equatorial Pacific, with deeper anomalies in the central equatorial Pacific, but shallower anomalies near both side boundaries. The time series of M1 (M2) exhibits the quasi-quadrennial (biennial) oscillation features of the EP (CP) El Niño events. In contrast to the SST-based indices (e.g., Niño-3 index and EMI), the M1 and M2 indices show a good capability to separate the type of El Niño events due to their time orthogonal relationship, and they can enhance the interannual periodicity contrast between the two types of El Niño events.

In addition, the changes of M1 and M2 indices reveal the feedbacks of equatorial Pacific thermocline fluctuations to the El Niño. It is found the thermocline fluctuations described by the D20 anomalies are influential during the life cycle of EP and CP El Niño events. The fluctuations propagate eastward before the mature phase of both EP and CP El Niño events. Moreover, the

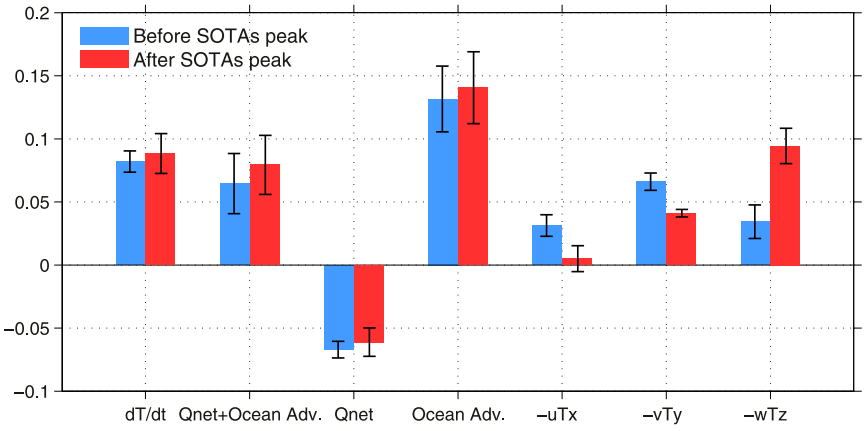

FIG. 10. Composite mixed layer temperature budget terms (°C month^{-1}) averaged over the central equatorial Pacific (5°S–5°N, 180°–120°W) 3 months before (blue bar) and after (red bar) the SOTAs peak for pure CP El Niño events, together with the corresponding composited standard errors as indicated by black lines. The seven bars denote the mixed layer temperature tendency, the summation of the surface heat flux term and ocean temperature advection, the surface heat flux term, the summation of the ocean temperature advection terms, and the individual zonal, meridional, and vertical advection terms, respectively.

eastward thermocline fluctuations extend more broadly, particularly for the CP El Niño events. This finding highlights the vitally important role of thermocline fluctuations in both El Niño events. M1 and M2 clearly indicate the physical significance on the interannual time scale, manifesting themselves as the dominant features of the thermocline fluctuations with respect to two types of El Niño. The time series of M1 and M2 provide us a benchmark to evaluate the amplitudes of two types El Niño due to their time independence.

In the case of CP El Niño events, we found that the air–sea interaction determines their establishment, but the thermocline feedback is vital for their further development. Before CP El Niño, the warming SSTAs prevail in the northeastern subtropical Pacific, then intrude into the tropics and merge with their counterparts from the western Pacific. Subsequently they produce the SSTAs warming in the central equatorial Pacific, which has been found to act as a predecessor to CP El Niño events (Yu et al. 2010; Yu and Kim 2011). Meanwhile, because of the arrival of downwelling equatorial Kelvin waves stimulated by the anomalous westerlies over the western equatorial Pacific, the warming SOTAs intensify and propagate eastward from the western equatorial Pacific to the central equatorial Pacific before the SOTA peak of CP El Niño events. Subsequently, the robust positive

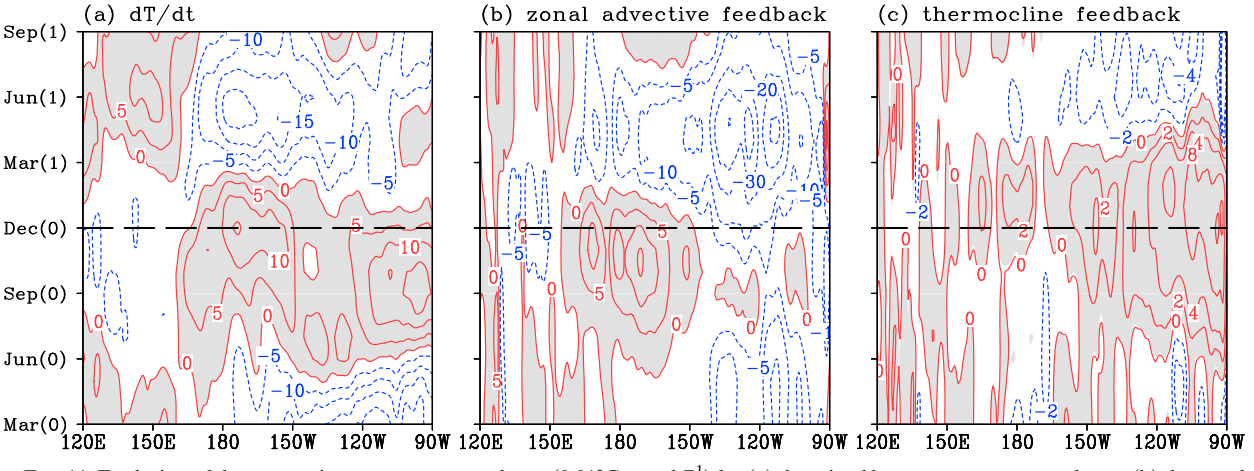

FIG. 11. Evolution of the composite temperature tendency (0.01°C month^{-1}) for (a) the mixed layer temperature tendency, (b) the zonal advective feedback, and (c) the thermocline feedback for the pure CP El Niño events. Fields are averaged over 5°S–5°N, and gray shading indicates the region of the positive temperature tendency. The ordinates denote lag months, where (0) indicates the pure CP El Niño year and (1) represents the following year.

SOTAs further expand upward and eastward, resulting in enhanced SSTAs in the central equatorial Pacific via the thermocline feedback. With the help of a mixed layer heat budget analysis, we further demonstrate that the zonal advective feedback contributes mainly to the development stage before the SOTA peak of CP El Niño events, while the thermocline adjustment processes are vital for the period after the SOTA peak of CP El Niño events.

It is noted the results might be different because of the methods. For instance, Ren and Jin (2013) suggested that thermocline feedback plays a dominant role in the growth and phase transitions of CP El Niño events, whereas the zonal advective feedback contributes mainly to their phase transitions. Wen et al. (2014) proposed that the enhanced off-equatorial thermocline plays an important role in the development of El Niño events after 1999. Nevertheless, all of the findings suggest that equatorial Pacific thermocline dynamics play a dominant role during the life cycle of the CP El Niño. Furthermore, the basin-mean equatorial thermocline depth exhibits a notable decadal variability in the Pacific (Fig. 1b) due to the equatorial Pacific surface wind stress forcing (Li and Ren 2012; Kosaka and Xie 2013). Therefore, more attention should be paid to its importance in the two types of El Niño cycles.

Our results are primarily from statistical analyses; the dynamics of equatorial thermocline fluctuations need a modeling study. In addition, here we mainly discussed M1 and M2; the physical meaning of the higher modes in the equatorial thermocline will be explored in future studies.

Acknowledgments. The authors gratefully acknowledged the valuable comments and suggestions given by the editor (Dr. Tim Li) and the anonymous reviewers, and also thank Dr. Boqi Liu for his constructive suggestions. This work is jointly supported by the Funds for Creative Research Groups of China (Grant 41521005), the Special Fund for Public Welfare Industry (GYHY201506013), the Strategic Priority Research Program of the Chinese Academy of Sciences (Grant XDA11010301), and the National Natural Science Foundation of China (Grants 41406033, 41475057, 41376024, 41676013) and the CAS/SAFEA International Partnership Program for Creative Research Teams.

APPENDIX

Mode Function Decomposition Method

The lowest-order mode (or mode 0) of the equatorial thermocline is a constant, $f_0 \equiv 1$, representing the mean depth of the equatorial thermocline. Therefore, the thermocline depth deviation from this basin-mean depth

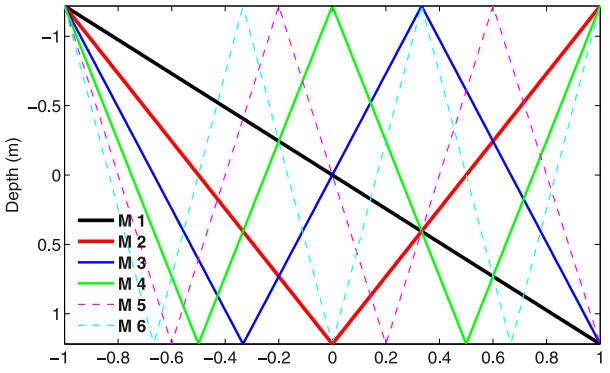

FIG. A1. First six normalized mode functions for the equatorial thermocline. Following the tradition in oceanography, the depth is positive in the downward direction.

can be decomposed into a series of mode functions. The mode functions are defined over the domain $[-1, +1]$, and they are orthogonal to each other, as a fundamental requirement. These modes start from a value of -1 at the left edge of the domain (i.e., $x = -1$) and consist of line segments that vary within the range $[-1, +1]$. Mode n has n zero-crossings. As a result, the first mode is a straight line from $(-1, -1)$ to $(+1, +1)$, and all other modes are composed of the straight line segments between -1 and $+1$, as shown in Fig. A1. The tradition in oceanography is to label depth as a positive value and define the downward direction as positive. This is opposite to the common practice in meteorology; however, in presenting the anomalous signals associated with the thermocline depth, this method can present the signals in a simple and accurate way.

These mode functions are further spatially normalized to a series of functions $f(x)$ satisfying the following unification constraints:

$$\int_{-1}^{1} f_i(x) f_j(x)\, dx = \delta_{ij} \quad (i, j \geq 1), \tag{A1}$$

where the subscripts i and j are the mode numbers, and δ is the Kronecker delta function. Regarding the temporal evolution of the decomposed modes, the main equatorial thermocline depth anomalies $D(x, t)$ averaged between 5°S and 5°N, defined over the nondimensional domain $x = [-1, +1]$, can be projected onto these mode function series for any given time t as follows:

$$D(x,t) = \sum_{i=1}^{\infty} a_i(t) f_i(x); \quad a_i(t) = \int_{-1}^{1} f_i(x) D(x,t)\, dx, \tag{A2}$$

where $a_i(t)$ is the time evolution for each mode i. The related code and data for the mode function decomposition method can be obtained online at https://github.com/xu-kang/MDF.

Figure A1 presents the visual image of the normalized structures of the first six mode functions. The mode functions are orthogonal to each other and have the same amplitude of 1.22; thus, in terms of thermocline depth variability, the amplitude of the contribution from each mode is $1.22a_i(t)$. As seen in Fig. A1, the spatial structure of the first mode (M1, depicted by a solid black line), clearly shows a basinwide east–west-tilted thermocline, with shoaling in the west and deepening in the east, which depicts the basic feature of classical EP El Niño events (Fig. A1). However, the second mode (M2, marked by the V-shaped red curve) has a deeper thermocline positioned in the central Pacific Ocean basin and a shallower thermocline on both side boundaries, representing the characteristic of CP El Niño events (Fig. A1). Therefore, this mode function decomposition method may provide a direct physical interpretation of the equatorial thermocline using only a few modes, and the first two leading modes have better capabilities in capturing and distinguishing the characteristics of the two types of El Niño events.

REFERENCES

Ashok, K., and T. Yamagata, 2009: Climate change: The El Niño with a difference. *Nature*, **461**, 481–484, doi:10.1038/461481a.

——, S. K. Behera, S. A. Rao, H. Weng, and T. Yamagata, 2007: El Niño Modoki and its possible teleconnection. *J. Geophys. Res.*, **112**, C11007, doi:10.1029/2006JC003798.

Behringer, D. W., and Y. Xue, 2004: Evaluation of the global ocean data assimilation system at NCEP: The Pacific Ocean. *Proc. Eighth Symp. on Integrated Observing and Assimilation Systems for Atmosphere, Oceans, and Land Surface*, Seattle, WA, Amer. Meteor. Soc., 2.3. [Available online at https://ams.confex.com/ams/pdfpapers/70720.pdf.]

Carton, J. A., B. S. Giese, and S. A. Grodsky, 2005: Sea level rise and the warming of the oceans in the Simple Ocean Data Assimilation (SODA) ocean reanalysis. *J. Geophys. Res.*, **110**, C09006, doi:10.1029/2004JC002817.

Chen, L., T. Li, S. K. Behera, and T. Doi, 2016: Distinctive precursory air–sea signals between regular and super El Niños. *Adv. Atmos. Sci.*, **33**, 996–1004, doi:10.1007/s00376-016-5250-8.

Chung, P., and T. Li, 2013: Interdecadal relationship between the mean state and El Niño types. *J. Climate*, **26**, 361–379, doi:10.1175/JCLI-D-12-00106.1.

Compo, G. P., and Coauthors, 2011: The Twentieth Century Reanalysis Project. *Quart. J. Roy. Meteor. Soc.*, **137**, 1–28, doi:10.1002/qj.776.

Gu, D., and S. G. H. Philander, 1997: Interdecadal climate fluctuations that depend on exchanges between the tropics and extratropics. *Science*, **275**, 805–807, doi:10.1126/science.275.5301.805.

Jin, F.-F., 1997: An equatorial ocean recharge paradigm for ENSO. Part I: Conceptual model. *J. Atmos. Sci.*, **54**, 811–829, doi:10.1175/1520-0469(1997)054<0811:AEORPF>2.0.CO;2.

Kang, I.-S., and J.-S. Kug, 2002: El Niño and La Niña sea surface temperature anomalies: Asymmetry characteristics associated with their wind stress anomalies. *J. Geophys. Res.*, **107**, 4372, doi:10.1029/2001JD000393.

Kao, H., and J. Yu, 2009: Contrasting eastern-Pacific and central-Pacific types of ENSO. *J. Climate*, **22**, 615–632, doi:10.1175/2008JCLI2309.1.

Kessler, W. S., 1990: Observations of long Rossby waves in the northern tropical Pacific. *J. Geophys. Res.*, **95**, 5183–5217, doi:10.1029/JC095iC04p05183.

Kim, W., S. Yeh, J. Kim, J. Kug, and M. Kwon, 2011: The unique 2009–2010 El Niño event: A fast phase transition of warm pool El Niño to La Niña. *Geophys. Res. Lett.*, **38**, L15809, doi:10.1029/2011GL048521.

Kosaka, Y., and S.-P. Xie, 2013: Recent global-warming hiatus tied to equatorial Pacific surface cooling. *Nature*, **501**, 403–407, doi:10.1038/nature12534.

Kug, J.-S., F.-F. Jin, and S.-I. An, 2009: Two types of El Niño events: Cold tongue El Niño and warm pool El Niño. *J. Climate*, **22**, 1499–1515, doi:10.1175/2008JCLI2624.1.

——, J. Choi, S. An, F. Jin, and A. T. Wittenberg, 2010: Warm pool and cold tongue El Niño events as simulated by the GFDL 2.1 coupled GCM. *J. Climate*, **23**, 1226–1239, doi:10.1175/2009JCLI3293.1.

Larkin, N. K., and D. E. Harrison, 2005: On the definition of El Niño and associated seasonal average U.S. weather anomalies. *Geophys. Res. Lett.*, **32**, L13705, doi:10.1029/2005GL022738.

Lee, T., and M. J. McPhaden, 2010: Increasing intensity of El Niño in the central-equatorial Pacific. *Geophys. Res. Lett.*, **37**, L14603, doi:10.1029/2010GL044007.

Li, G., and B. Ren, 2012: Evidence for strengthening of the tropical Pacific Ocean surface wind speed during 1979–2001. *Theor. Appl. Climatol.*, **107**, 59–72, doi:10.1007/s00704-011-0463-3.

Li, T., T. F. Hogan, and C. Chang, 2000: Dynamic and thermodynamic regulation of ocean warming. *J. Atmos. Sci.*, **57**, 3353–3365, doi:10.1175/1520-0469(2000)057<3353:DATROO>2.0.CO;2.

——, Y. Zhang, E. Lu, and D. Wang, 2002: Relative role of dynamic and thermodynamic processes in the development of the Indian Ocean dipole: An OGCM diagnosis. *Geophys. Res. Lett.*, **29**, 2110, doi:10.1029/2002GL015789.

Li, X., C. Li, J. Ling, and Y. Tan, 2015: The relationship between contiguous El Niño and La Niña revealed by self-organizing maps. *J. Climate*, **28**, 8118–8134, doi:10.1175/JCLI-D-15-0123.1.

McPhaden, M. J., S. E. Zebiak, and M. H. Glantz, 2006: ENSO as an integrating concept in Earth science. *Science*, **314**, 1740–1745, doi:10.1126/science.1132588.

Meinen, C. S., and M. J. McPhaden, 2000: Observations of warm water volume changes in the equatorial Pacific and their relationship to El Niño and La Niña. *J. Climate*, **13**, 3551–3559, doi:10.1175/1520-0442(2000)013<3551:OOWWVC>2.0.CO;2.

North, G. R., T. L. Bell, R. F. Cahalan, and F. J. Moeng, 1982: Sampling errors in the estimation of empirical orthogonal functions. *Mon. Wea. Rev.*, **110**, 699–706, doi:10.1175/1520-0493(1982)110<0699:SEITEO>2.0.CO;2.

Pedlosky, J., 1987: An inertial theory of the equatorial undercurrent. *J. Phys. Oceanogr.*, **17**, 1978–1985, doi:10.1175/1520-0485(1987)017<1978:AITOTE>2.0.CO;2.

Rayner, N. A., D. E. Parker, E. B. Horton, C. K. Folland, L. V. Alexander, D. P. Rowell, E. C. Kent, and A. Kaplan, 2003: Global analyses of sea surface temperature, sea ice, and night marine air temperature since the late nineteenth century. *J. Geophys. Res.*, **108**, 4407, doi:10.1029/2002JD002670.

Ren, H., and F. Jin, 2011: Niño indices for two types of ENSO. *Geophys. Res. Lett.*, **38**, L04704, doi:10.1029/2010GL046031.

——, and ——, 2013: Recharge oscillator mechanisms in two types of ENSO. *J. Climate*, **26**, 6506–6523, doi:10.1175/JCLI-D-12-00601.1.

Su, J., T. Li, and R. Zhang, 2014: The initiation and developing mechanisms of central Pacific El Niños. *J. Climate*, **27**, 4473–4485, doi:10.1175/JCLI-D-13-00640.1.

Trenberth, K. E., and D. P. Stepaniak, 2001: Indices of El Niño evolution. *J. Climate*, **14**, 1697–1701, doi:10.1175/1520-0442(2001)014<1697:LIOENO>2.0.CO;2.

Wang, C., and X. Wang, 2013: Classifying El Niño Modoki I and II by different impacts on rainfall in southern China and typhoon tracks. *J. Climate*, **26**, 1322–1338, doi:10.1175/JCLI-D-12-00107.1.

Wang, L., T. Li, and T. Zhou, 2012: Intraseasonal SST variability and air–sea interaction over the Kuroshio Extension region during boreal summer. *J. Climate*, **25**, 1619–1634, doi:10.1175/JCLI-D-11-00109.1.

Wang, X., and C. Wang, 2014: Different impacts of various El Niño events on the Indian Ocean dipole. *Climate Dyn.*, **42**, 991–1005, doi:10.1007/s00382-013-1711-2.

Wen, C., A. Kumar, Y. Xue, and M. J. McPhaden, 2014: Changes in tropical Pacific thermocline depth and their relationship to ENSO after 1999. *J. Climate*, **27**, 7230–7249, doi:10.1175/JCLI-D-13-00518.1.

Weng, H., K. Ashok, S. K. Behera, S. A. Rao, and T. Yamagata, 2007: Impacts of recent El Niño Modoki on dry/wet conditions in the Pacific rim during boreal summer. *Climate Dyn.*, **29**, 113–129, doi:10.1007/s00382-007-0234-0.

Wyrtki, K., 1989: Some thoughts about the west Pacific warm pool. *Proc. West Pacific Int. Meeting and Workshop on TOGA COARE*, Nouméa, New Caledonia, Office de la recherche scientifique et technique outre-mer (ORSTOM), 99–109.

Xiang, B., B. Wang, and T. Li, 2013: A new paradigm for the predominance of standing central Pacific warming after the late 1990s. *Climate Dyn.*, **41**, 327–340, doi:10.1007/s00382-012-1427-8.

Xie, S.-P., and S. G. H. Philander, 1994: A coupled ocean–atmosphere model of relevance to the ITCZ in the eastern Pacific. *Tellus*, **46A**, 340–350, doi:10.3402/tellusa.v46i4.15484.

Xu, K., C. Zhu, and J. He, 2012: Linkage between the dominant modes in Pacific subsurface ocean temperature and the two type ENSO events. *Chin. Sci. Bull.*, **57**, 3491–3496, doi:10.1007/s11434-012-5173-4.

——, ——, and ——, 2013: Two types of El Niño-related Southern Oscillation and their different impacts on global land precipitation. *Adv. Atmos. Sci.*, **30**, 1743–1757.

——, J. Su, and C. Zhu, 2014: The natural oscillation of two types of ENSO events based on analyses of CMIP5 model control runs. *Adv. Atmos. Sci.*, **31**, 801–813, doi:10.1007/s00376-013-3153-5.

——, C.-Y. Tam, C. Zhu, B. Liu, and W. Wang, 2017: CMIP5 projections of two types of El Niño and their related tropical precipitation in the twenty-first century. *J. Climate*, **30**, 849–864, doi:10.1175/JCLI-D-16-0413.1.

Yeh, S., J. Kug, B. Dewitte, M. Kwon, B. P. Kirtman, and F. Jin, 2009: El Niño in a changing climate. *Nature*, **461**, 511–514, doi:10.1038/nature08316.

Yu, J.-Y., and H.-Y. Kao, 2007: Decadal changes of ENSO persistence barrier in SST and ocean heat content indices: 1958–2001. *J. Geophys. Res.*, **112**, D13106, doi:10.1029/2006JD007654.

——, and S. T. Kim, 2011: Relationships between extratropical sea level pressure variations and the central Pacific and eastern Pacific types of ENSO. *J. Climate*, **24**, 708–720, doi:10.1175/2010JCLI3688.1.

——, H.-Y. Kao, and T. Lee, 2010: Subtropics-related interannual sea surface temperature variability in the central equatorial Pacific. *J. Climate*, **23**, 2869–2884, doi:10.1175/2010JCLI3171.1.

——, ——, ——, and S. T. Kim, 2011: Subsurface ocean temperature indices for central-Pacific and eastern-Pacific types of El Niño and La Niña events. *Theor. Appl. Climatol.*, **103**, 337–344, doi:10.1007/s00704-010-0307-6.

——, Y. Zou, S. T. Kim, and T. Lee, 2012: The changing impact of El Niño on US winter temperatures. *Geophys. Res. Lett.*, **39**, L15702, doi:10.1029/2012GL052483.

Zhang, W., F. Jin, and A. Turner, 2014: Increasing autumn drought over southern China associated with ENSO regime shift. *Geophys. Res. Lett.*, **41**, 4020–4026, doi:10.1002/2014GL060130.

——, Y. Wang, F. Jin, M. F. Stuecker, and A. G. Turner, 2015: Impact of different El Niño types on the El Niño/IOD relationship. *Geophys. Res. Lett.*, **42**, 8570–8576, doi:10.1002/2015GL065703.